Free-surface thin-film flows over topography: influence of inertia and viscoelasticity

SERGEY SAPRYKIN[1], RUDY J. KOOPMANS[2]
AND SERAFIM KALLIADASIS[1]†

[1]Department of Chemical Engineering, Imperial College London, London, SW7 2AZ, UK
[2]Core R&D, Dow Benelux BV, 4530 AA Terneuzen, The Netherlands

We consider viscoelastic flows over topography in the presence of inertia. Such flows are modelled by an integral-boundary-layer approximation of the equations of motion and wall/free-surface boundary conditions. Steady states for flows over a step-down in topography are characterized by a capillary ridge immediately before the entrance to the step. A similar capillary ridge has also been observed for non-inertial Newtonian flows over topography. The height of the ridge is found to be a monotonically decreasing function of the Deborah number. Further, we examine the interaction between capillary ridges and excited non-equilibrium inertia/viscoelasticity-driven solitary pulses. We demonstrate that ridges have a profound influence on the drainage dynamics of such pulses: they accelerate the drainage process so that once the pulses pass the topographical feature they become equilibrium ones and are no longer excited.

1. Introduction

Free-surface thin-film flows over topography have recently received considerable attention and have been the focus of several works. We briefly review some of these studies. Kalliadasis, Bielarz & Homsy (2000) used the long-wave (LWE) lubrication approximation to perform a systematic parametric investigation of steady-state solutions for flows over topographical features such as single steps (steps-down and -up) and finite features (trenches and mounds). Mazouchi & Homsy (2001) solved for the steady states of the full Stokes equation for flows over topography and demonstrated that the lubrication theory provides a good approximation of the flows for sufficiently small values of the capillary number. On the other hand, Gramlich *et al.* (2002) examined the possibility of levelling flows over topography by means of thermocapillary Marangoni stresses produced by localized heaters on the topographical substrate. The stability of free-surface thin-film flows over topographical features was addressed by Kalliadasis & Homsy (2001) who examined in detail the spectrum of the linearized operator of the system that governs the evolution of infinitesimal disturbances in the transverse direction. They demonstrated that flows over topographical features are asymptotically stable and they also performed an energy analysis of the associated eigenvalue problem to reveal the stability mechanism for such flows. These theoretical predictions were found to be in agreement with fully

† Author to whom correspondence should be addressed: S.Kalliadasis@imperial.ac.uk

nonlinear time-dependent computations using the two-dimensional LWE (Bielarz & Kalliadasis 2003). Davis & Troian (2005) undertook a detailed non-modal analysis of the linear stability problem considered by Kalliadasis & Homsy (2001) to investigate the possibility of transient amplification associated with the non-normality of the disturbance operator. A minimal transient amplification of perturbations was found to occur, thus confirming the predictions of the linear stability analysis.

In this study, we consider viscoelastic free-surface thin-film flows over topography by using the flow over a step-down as a model system. Viscoelasticity is modelled with a relatively simple constitutive equation, the convected Maxwell model. There is particular emphasis on the influence of inertia.

For inertia-driven flows on planar substrates, it is well known that the solitary wave solution branches of LWE for the speed of the waves as a function of Reynolds number show branch multiplicity and limit points at $O(1)$ Reynolds numbers above which solitary waves do not exist (see e.g. Pumir, Manneville & Pomeau 1983). Time-dependent computations by Pumir *et al.* (1983) showed that LWE exhibits a finite-time blow-up behaviour for a sufficiently large set of smooth initial data when this equation is integrated in regions of the parameter space where solitary waves do not exist. Obviously this behaviour is unrealistic, and marks the failure of LWE in the region of moderate Reynolds numbers. The connection between the absence of solitary wave solutions and finite-time blow up has been scrutinized by Rosenau, Oron & Hyman (1992) and Oron & Gottlieb (2002) and further investigated by Scheid *et al.* (2004).

On the other hand, the so called integral-boundary-layer (IBL) approximation developed for inertia-driven flows on planar substrates by Shkadov (1967, 1968) has no turning points and predicts the continuing existence of solitary waves for all Reynolds numbers. This approximation combines the boundary-layer approximation of the Navier–Stokes equation, assuming a self-similar parabolic profile beneath the film and long waves on the interface, with the Kármán–Pohlhausen averaging method in boundary-layer theory. This procedure results in a two-equation model for the evolution in time and space of the free surface and local flow rate.

Here we extend Shkadov's IBL approximation to inertia-driven viscoelastic flows over topography. The approximation is derived by assuming weak topography and viscoelasticity. The final model is a system of two nonlinear partial differential equations for the evolution in time and space of the local thickness relative to the topography and local flow rate. We examine both steady states and time-dependent flows. We also investigate the interaction of viscoelastic solitary pulses with the steady states.

2. Problem definition, scalings and governing equations

We consider free-surface thin-film flows over topography using the flow over a step-down as a model system. Figure 1 shows the flow situation. A thin viscous fluid of viscosity μ (to be defined more precisely later), surface tension σ, density ρ and thickness h_0 is flowing over a step of depth D and characteristic scale δ. The ratio D/δ measures the steepness of the step while for fixed D the steepness is determined by δ only. The fluid is driven by a flux Uh_0 with U and h_0 the characteristic velocity and Nusselt flat-film thickness, respectively, far from the feature. This flux is due to an external body force such as the Coriolis force (relevant to centrifugal spin coating) or gravity. To fix ideas we consider here the case of a gravitationally driven flow with a vertical substrate. U then corresponds to $\rho g h_0^2/\mu$, the
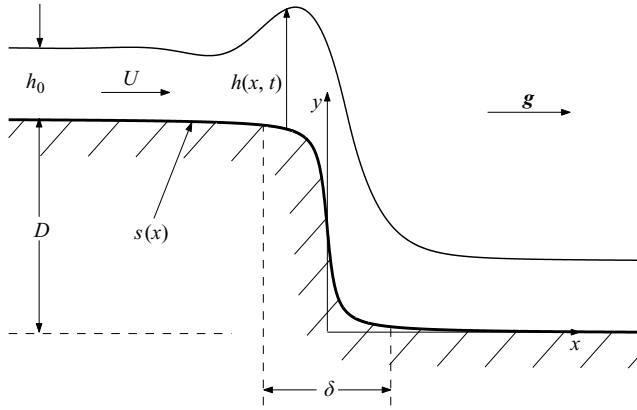
FIGURE 1. Flow over a step-down in topography: a fluid is flowing with a characteristic velocity U over a surface feature. The relative film thickness is $h(x, t)$ with respect to an orthogonal coordinate system (x, y) with origin on the step-down. The film thickness far from the feature is h_0. The solid substrate has a shape $s(x)$, a depth D and a characteristic scale δ.

characteristic velocity for viscous gravitational drainage for a film falling down a vertical substrate.

The governing equations are the Navier–Stokes and continuity:

$$\rho(\partial_t + \boldsymbol{v} \cdot \boldsymbol{\nabla})\boldsymbol{v} = -\boldsymbol{\nabla} p - \boldsymbol{\nabla} \cdot \boldsymbol{\tau} + \rho \boldsymbol{g}, \qquad (2.1a)$$

$$\boldsymbol{\nabla} \cdot \boldsymbol{v} = 0, \qquad (2.1b)$$

where $\boldsymbol{\nabla} = (\partial_x, \partial_y)$, $\boldsymbol{v} = (u, v)$ is the fluid velocity vector, $\boldsymbol{g} = (g, 0)$, p is the fluid pressure and

$$\boldsymbol{\tau} = \begin{bmatrix} \tau_{xx} & \tau_{xy} \\ \tau_{yx} & \tau_{yy} \end{bmatrix}$$

is the deviatoric stress tensor.

These equations are subject to the following boundary conditions. On the wall we have the usual no-slip boundary condition:

$$\boldsymbol{v} = 0 \quad \text{on} \quad y = s(x). \qquad (2.2a)$$

On the interface $y = H(x, t) \equiv s(x) + h(x, t)$ we have the kinematic boundary condition along with the normal and tangential stress balances

$$\partial_t h + u\partial_x H = v, \quad -p + (\boldsymbol{\tau} \cdot \boldsymbol{n}) \cdot \boldsymbol{n} = 2\sigma K(H), \quad (\boldsymbol{\tau} \cdot \boldsymbol{n}) \cdot \boldsymbol{t} = 0, \qquad (2.2b)$$

where, without loss of generality, the pressure of the surrounding gas phase has been set equal to zero. Also, $\boldsymbol{n}$ and $\boldsymbol{t}$ are unit vectors, normal (outward pointing) and tangential to the interface, respectively, defined from $\boldsymbol{n} = n^{-1}(-\partial_x H, 1)$, $\boldsymbol{t} = n^{-1}(1, \partial_x H)$ where $n = (1 + (\partial_x H)^2)^{1/2}$. Finally, $K(H) = -(1/2)\boldsymbol{\nabla} \cdot \boldsymbol{n}$ is the curvature of the interface.

We choose to model the polymeric stresses with an Oldroyd-B constitutive equation which has been used extensively to model the viscoelastic behaviour of a wide variety of flows (e.g Bird, Armstrong & Hassager 1987; Spaid & Homsy 1994, 1996):

$$\boldsymbol{\tau} + \lambda_1 \boldsymbol{\tau}_{(1)} = -\mu \left(\boldsymbol{d}_{(1)} + \lambda_2 \boldsymbol{d}_{(2)} \right) \qquad (2.3a)$$

where $\lambda_{1,2}$ are the relaxation and retardation times, respectively, μ is the zero-shear-rate viscosity and $\boldsymbol{\tau}_{(1)}$ denotes the convected time derivative of the stress tensor

defined as

$$\boldsymbol{\tau}_{(1)} = (\partial_t + \boldsymbol{v}\cdot\nabla)\boldsymbol{\tau} - [(\nabla\boldsymbol{v})^t\cdot\boldsymbol{\tau} + \boldsymbol{\tau}\cdot(\nabla\boldsymbol{v})]. \tag{2.3b}$$

$\boldsymbol{d}_{(1,2)}$ denote the first and second rate-of-strain tensors, respectively, defined as

$$\boldsymbol{d}_{(1)} \equiv \boldsymbol{d} \tag{2.3c}$$

and

$$\boldsymbol{d}_{(2)} = (\partial_t + \boldsymbol{v}\cdot\nabla)\boldsymbol{d}_{(1)} - \left[(\nabla\boldsymbol{v})^t\cdot\boldsymbol{d}_{(1)} + \boldsymbol{d}_{(1)}\cdot(\nabla\boldsymbol{v})\right], \tag{2.3d}$$

where

$$\boldsymbol{d} = (\nabla\boldsymbol{v}) + (\nabla\boldsymbol{v})^t \tag{2.3e}$$

is the rate-of-strain tensor.

For simplicity, we shall take $\lambda_2 = 0$ and $\lambda_1 \equiv \lambda$. In this case, (2.3) simplifies to:

$$\tau_{xx} + \lambda(\partial_t + \boldsymbol{v}\cdot\nabla)\tau_{xx} - 2\lambda(\tau_{xx}\partial_x u + \tau_{yx}\partial_y u) = -2\mu\partial_x u, \tag{2.4a}$$

$$\tau_{yx} + \lambda(\partial_t + \boldsymbol{v}\cdot\nabla)\tau_{yx} - \lambda(\tau_{xx}\partial_x v + \tau_{yy}\partial_y u) = -\mu(\partial_y u + \partial_x v), \tag{2.4b}$$

$$\tau_{yy} + \lambda(\partial_t + \boldsymbol{v}\cdot\nabla)\tau_{yy} - 2\lambda(\tau_{xy}\partial_x v + \tau_{yy}\partial_y v) = -2\mu\partial_y v. \tag{2.4c}$$

The Oldroyd-B constitutive model then becomes the 'convected Maxwell model' which has been widely used for viscoelastic flow calculations because of its simplicity (Bird *et al.* 1987). Setting $\lambda = 0$ in (2.4) retrieves the Newtonian constitutive equation.

We now introduce the non-dimensionalization

$$\left.\begin{aligned} &(x, \delta) \to \ell(x, \delta), \quad (y, h, s) \to h_0(y, h, s), \quad t \to \frac{\ell}{U}t, \quad u \to Uu, \quad v \to \frac{Uh_0}{\ell}v \\ &p \to \frac{\sigma h_0}{\ell^2}p, \quad \tau_{xx} \to \frac{\mu U \ell}{h_0^2}\tau_{xx}, \quad \tau_{yx} \to \frac{\mu U}{h_0}\tau_{yx}, \quad \tau_{yy} \to \frac{\mu U}{\ell}\tau_{yy}, \end{aligned}\right\} \tag{2.5}$$

where ℓ is a characteristic lengthscale in the streamwise direction set up by the flow far from the topographical feature. Time scales with the time in which an interfacial fluid particle transverses a distance ℓ. The scale for the y-component of the velocity v is determined by the continuity equation in (2.1b), $\partial_y v \sim \partial_x u$ or $v \sim Uh_0/\ell$. The scale for the pressure is obtained by balancing the pressure to the usual interfacial streamwise curvature gradient due to surface tension in the normal stress balance (2.2b), $p \sim \sigma \partial_{x^2} h$ or $p \sim \sigma h_0/\ell^2$. The choice of the scales for the stresses is discussed in Appendix A. These scales coincide with those used by Khayat (2000) and Zhang, Matar & Craster (2002).

In terms of the above non-dimensionalization, the Navier–Stokes and continuity equations in (2.1) contain three dimensionless parameters: the film parameter $\epsilon = h_0/\ell$, the Reynolds number $Re = h_0 U\rho/\mu$ and the capillary number $Ca = \mu U/\sigma$. Balancing now in the streamwise component of the Navier–Stokes equation the streamwise pressure gradient with the stress gradients and the body force gives $\epsilon \sim Ca^{1/3}$ or $\ell \sim h_0/Ca^{1/3}$. Hence, ℓ is the *capillary scale* introduced for flows over topography by Kalliadasis *et al.* (2000) and is indeed determined by the conditions far from the feature. In Kalliadasis *et al.* (2000), the capillary scale was obtained by simply balancing mean flow to the capillary force term in the LWE equation for the evolution of the free surface in the absence of inertia and viscoelasticity: $(U/h_0^2)\partial_x(h^3) \sim (\sigma/\mu)\partial_x(h^3\partial_{x^3}H)$ which gives $h_0/\ell \sim Ca^{1/3}$. The advantage of this scale is that the LWE equation for the evolution of the free surface in the absence of inertia and viscoelasticity is free of parameters (see also the discussion in Mazouchi & Homsy (2001) who solved numerically the full Stokes equations and established self-similarity of the profiles for small Ca when the variable $xCa^{1/3}$ was used as an

horizontal length). Note that an alternative scaling obtained by balancing gravity directly with the viscous friction in the streamwise momentum equation can also be used (see e.g. Ruyer-Quil *et al.* 2005).

The Navier–Stokes and continuity equations in (2.1) then become:

$$R(\partial_t u + u\partial_x u + v\partial_y u) = -\partial_x p - \partial_x \tau_{xx} - \partial_y \tau_{yx} + 1, \qquad (2.6a)$$

$$RCa^{2/3}(\partial_t v + u\partial_x v + v\partial_y v) = -\partial_y p - Ca^{2/3}(\partial_x \tau_{yx} + \partial_y \tau_{yy}), \qquad (2.6b)$$

$$\partial_x u + \partial_y v = 0, \qquad (2.6c)$$

where R is a modified Reynolds number defined as $R = ReCa^{1/3}$. These equations are subject to the wall boundary condition,

$$u = v = 0 \quad \text{on} \quad y = s(x), \qquad (2.7a)$$

and interfacial boundary conditions on $y = H(x, t)$,

$$\partial_t h + u\partial_x H = v, \qquad (2.7b)$$

$$-p + Ca^{2/3}\tau_{xx}\frac{(\partial_x H)^2}{1 + Ca^{2/3}(\partial_x H)^2} - 2Ca^{2/3}\tau_{yx}\frac{\partial_x H}{1 + Ca^{2/3}(\partial_x H)^2}$$

$$+ Ca^{2/3}\tau_{yy}\frac{1}{1 + Ca^{2/3}(\partial_x H)^2} = \frac{\partial_{x^2} H}{\left(1 + Ca^{2/3}(\partial_x H)^2\right)^{3/2}}, \quad (2.7c)$$

$$-\tau_{xx}\partial_x H + \tau_{yx}\left(1 - Ca^{2/3}(\partial_x H)^2\right) + Ca^{2/3}\tau_{yy}\partial_x H = 0. \qquad (2.7d)$$

Finally, the dimensionless version of the constitutive model becomes

$$\tau_{xx} + De(\partial_t \tau_{xx} + u\partial_x \tau_{xx} + v\partial_y \tau_{xx} - 2\tau_{xx}\partial_x u - 2\tau_{yx}\partial_y u) = -2Ca^{2/3}\partial_x u, \qquad (2.8a)$$

$$\tau_{yx} + De(\partial_t \tau_{yx} + u\partial_x \tau_{yx} + v\partial_y \tau_{yx} - \tau_{xx}\partial_x v - \tau_{yy}\partial_y u) = -\partial_y u - Ca^{2/3}\partial_x v, \qquad (2.8b)$$

$$\tau_{yy} + De(\partial_t \tau_{yy} + u\partial_x \tau_{yy} + v\partial_y \tau_{yy} - 2\tau_{xy}\partial_x v - 2\tau_{yy}\partial_y v) = -2\partial_y v, \qquad (2.8c)$$

where $De = \lambda/(\ell/U)$ is the Deborah number which expresses the ratio of the time scale for the viscoelastic effects to the hydrodynamic time scale.

Typical values of the various dimensional parameters in applications with both Newtonian and viscoelastic fluids are (Stillwagon & Larson 1988, 1990; Fraysse & Homsy 1994; Spaid & Homsy 1994; Messé & Decré 1997; Fernandez-Parent, Lammers & Decré 1998; Argyriadi, Vlachogiannis & Bontozoglou 2006): $\mu = 1 - 5000 \, \text{cp}$, $\sigma = 20 - 50 \, \text{dyn cm}^{-1}$, $\rho \approx 1 \, \text{g cm}^{-3}$, $h_0 = 0.5 \, \mu\text{m} - 1 \, \text{mm}$, $\tilde{D} = 1 \, \mu\text{m} - 1 \, \text{mm}$, $\tilde{\delta} \approx 0.01 \, \mu\text{m}$, $U = 10^{-6} - 1 \, \text{cm s}^{-1}$ and $\lambda \lesssim 1 \, \text{s}$ – tildes are introduced to distinguish between dimensional and dimensionless quantities. These give the following wide ranges of dimensional and dimensionless parameters which cover the widest possible range of flows: $Ca = 2 \times 10^{-10} - 2.5$, $\ell = 0.5 \, \mu\text{m} - 170 \, \text{cm}$, $De = 6 \times 10^{-9} - 3 \times 10^4$, $D = 10^{-3} - 2 \times 10^3$, $\delta = 6 \times 10^{-9} - 3 \times 10^{-2}$ and $Re = 10^{-12} - 10$.

3. Long-wave assumption

Since surface tension is, in general, large, waves on the surface are typically long compared to the film thickness, thus justifying a long-wave assumption corresponding to a slowly varying interface in time and space. Hence, ℓ is a long length scale in the streamwise direction so that $\epsilon = h_0/\ell \equiv Ca^{1/3} \ll 1$, representing a typical slope of the film away from the topographical feature.

We shall also make the additional assumption of a weak topography. More specifically,

$$Ca^{1/3}\partial_x H \ll 1 \quad \text{or} \quad Ca^{1/3}\partial_x s \ll 1,$$

which allows us to neglect terms of $O(Ca^{2/3}(\partial_x H)^2)$ in our governing equations. The slope of the topography in the immediate vicinity of the step can be easily estimated to be:

$$x = O(\delta), \quad \partial_x s \sim D/\delta \Rightarrow Ca^{1/3}\partial_x s \sim Ca^{1/3}(\ell/h_0)(\tilde{D}/\tilde{\delta}) = \tilde{D}/\tilde{\delta}.$$

The condition $Ca^{1/3}\partial_x s \ll 1$ then gives $\tilde{D}/\tilde{\delta} \ll 1$ and $D/\delta \ll Ca^{-1/3}$ so that D/δ can be large, but it can only increase at a slower rate to $Ca^{-1/3}$. However, $\partial_{\tilde{x}}\tilde{s} \sim \tilde{D}/\tilde{\delta}$, which is small. In other words, the topography slope in terms of dimensional variables is small, even though the steepness D/δ can be large. For fixed D, the condition $D/\delta \gg 1$ requires $\delta = \tilde{\delta}/\ell \ll 1$ or $\ell \gg \tilde{\delta}(\gg \tilde{D})$, i.e. the two scales ℓ and $\tilde{\delta}$ are well separated, allowing us to investigate the limit of small δ (for fixed D).

We now turn to the slope of the deviation height in the immediate vicinity of the step. This slope can be large simply because in this region, x in $\partial_x h$ varies within a distance of $O(\delta)$ instead of $O(\ell)$ far from the feature. As a matter of fact, $\partial_x h$ can be as large as $\partial_x s \sim D/\delta$, as we shall confirm in §5.1. From the above, $\partial_{\tilde{x}}\tilde{h} \sim \partial_{\tilde{x}}\tilde{s} \sim \tilde{D}/\tilde{\delta}$, and hence the slope of the deviation height in terms of dimensional variables is still small, as it should be in order to sustain the long-wave assumption. On the other hand, far from the feature

$$x \gg \delta, \quad D/\delta \gg 1 \Rightarrow \tilde{D}/h_0 \gg \tilde{\delta}/\ell \Rightarrow \tilde{D}/\tilde{\delta} \gg h_0/\ell \Rightarrow \partial_{\tilde{x}}\tilde{h} \ll \partial_{\tilde{x}}\tilde{s}(\ll 1)$$

there, so that in terms of dimensional variables, the deviation height slope over the feature is much larger than the deviation height slope away from the feature.

We note here that the slope $\partial_x h$ of the deviation height is everywhere $O(1)$, or equivalently $\partial_{\tilde{x}}\tilde{h} = O(\epsilon)$, the formal order of the slope, except for the immediate vicinity of the step where it increases to $\tilde{D}/\tilde{\delta}$. As awkward as it may appear, this 'inconsistency' is not specific to the topography problem, and occurs frequently in thin-film studies, e.g. the problem of a film falling down a planar inclined wall (Chang 1994) where $\partial_x h$ can be large at the front of steep solitary waves, thus preventing the waves from breaking. Similarly in our case, $\partial_{\tilde{x}}\tilde{h}$ has its formal order throughout the domain except in the immediate vicinity of the step where it becomes larger than its formal order in order to balance the topography contribution $\partial_{\tilde{x}}\tilde{s}$ and hence prevent our standing wave over the topographical feature from 'breaking'.

4. IBL approximation

For a film falling down a planar substrate the starting point of the IBL approach is to assume long-waves in the x-direction. Based then on our discussion in the previous section, we neglect terms of $O(Ca^{2/3}, Ca^{2/3}(D/\delta)^2)$ and higher. Hence, to leading order, the y-component of the equation of motion (2.6b) and normal stress balance (2.7c) are $\partial_y p = 0$ and $p = -\partial_{x^2}H$ on $y = H(x,t)$. The pressure distribution can then be easily obtained to be $p = -\partial_{x^2}H$ which when substituted in the x-momentum equation (2.6a) yields

$$R(\partial_t u + u\partial_x u + v\partial_y u) = \partial_{x^3}H - \partial_x \tau_{xx} - \partial_y \tau_{yx} + 1. \tag{4.1}$$

We now turn to the constitutive model in (2.8). A substantial simplification of this model can be achieved by assuming $De \ll 1$. The viscoelastic effects are then adiabatically slaved to the hydrodynamics. This assumption has been made frequently

in the study of viscoelastic thin-film flow problems (Spaid & Homsy 1994, 1996; Zhang *et al.* 2002) as it allows the 'inversion' of the nonlinear constitutive viscoleastic model to obtain explicit expressions for the stresses. At first-order in De, we obtain from (2.8) the following approximation for the stresses:

$$\tau_{xx} = -2De(\partial_y u)^2, \tag{4.2a}$$

$$\tau_{yx} = -\partial_y u + De[\partial_t \partial_y u + u\partial_x \partial_y u + v\partial_{yy}u - 2(\partial_y u)(\partial_y v)], \tag{4.2b}$$

$$\tau_{yy} = -2\partial_y v + O(De), \tag{4.2c}$$

where for τ_{yy} only the $O(1)$ term is required for the analysis to follow. Hence, the memory effects associated with viscoelasticity are postponed to $O(De)$. Note that since we neglect terms of $O(Ca^{2/3}, Ca^{2/3}(D/\delta)^2)$ but we keep terms of $O(De)$, we must have $Ca^{2/3}, Ca^{2/3}(D/\delta)^2 \ll De$. This is sufficient to determine the level of truncation of both De- and Ca-expansions and a precise relative order between De and Ca is not required. However, the relative order between De and $R = ReCa^{1/3}$ determines the relative importance between viscoelasticity and inertia. For example, if $De \gg Ca^{1/3}$ then for $O(1)$, or even moderate values of Re, De is large compared to R and viscoelasticity dominates over inertia.

An *ad hoc* and convenient simplification of our system can be made by assuming that the velocity profile has the self-similar form

$$u = \frac{3q}{h} \left(\eta - \tfrac{1}{2}\eta^2 \right) \tag{4.3a}$$

where

$$\eta = \frac{y - s(x)}{h(x, t)}, \qquad q = \int_s^H u\,\mathrm{d}y, \tag{4.3b}$$

with η a natural similarity variable to use – as the boundary conditions in terms of η are applied at $\eta = 0$ and $\eta = 1$ – and with q the flow rate in the streamwise direction. The continuity equation then in (2.6c) along with the no-slip condition in (2.7a) can be used to obtain v, $v = -\int_s^y \partial_x u\,\mathrm{d}y'$. For $s = 0$, (4.3) is the velocity profile introduced by Shkadov (1967, 1968) for Newtonian films falling down planar substrates.

The parabolic velocity distribution for u in (4.3a) is the simplest possible test function which satisfies all boundary conditions. Indeed, it satisfies the no-slip condition (2.7a) and also gives $\partial_y u|_{y=H} = 0$. Hence from (4.2a), $\tau_{xx}|_{y=H} = 0$ and from (4.2b), $\tau_{yx}|_{y=H} = [(\partial_t + u\partial_x + v\partial_y)\partial_y u]_{y=H}$. This last quantity vanishes since $\partial_y u$ is always equal to zero at any point on the interface so that its time derivative following any material point on the interface (which is merely the 'material derivative') is obviously equal to zero. As a consequence both the x-directed normal stress and shear stress on the interface vanish and hence the tangential stress balance in (2.7d) is trivially satisfied. In addition, the integral of the u-profile in (4.3a) with respect to y (or the similarity variable η) gives the flow rate q, as it should.

The introduction of the test function (4.3a) yields the following residual for the momentum equation (4.1):

$$\mathscr{R} = R(\partial_t u + u\partial_x u + v\partial_y u) - \partial_{x^3}H + \partial_x \tau_{xx} + \partial_y \tau_{yx} - 1. \tag{4.4}$$

Following the studies by Ruyer-Quil & Manneville (2000, 2002) for Newtonian films falling down planar substrates, the momentum residual can be minimized via a weighted residual approach that would yield a constraint on q and hence a closure

for the system,

$$\langle w, \mathscr{R} \rangle = 0 \qquad (4.5)$$

where w is the weight function and the inner product is defined as $\langle f, g \rangle = \int_0^1 fg \, \mathrm{d}\eta$ for any two functions f and g with appropriate boundary conditions.

Specifying the weight function fixes the particular weighted-residual method being used. For Newtonian films falling down planar substrates, Ruyer-Quil & Manneville (2000, 2002) showed that the Kármán–Pohlhausen averaging method employed by Shkadov (1967, 1968) can be viewed as a special weighted-residual method with $w \equiv 1$. This is the weight function we adopt here. The same weight function was also adopted by Kalliadasis *et al.* (2003*a, b*) for Newtonian films falling down heated planar substrates, whereas for the same problem, high-order weighted-residuals approximations have been developed by Ruyer-Quil *et al.* (2005) and Scheid *et al.* (2005).

Substituting then the test function (4.3*a*) into (4.5), performing integrations by parts and using the no-slip condition (2.7*a*), continuity equation (2.6*c*) and kinematic condition (2.7*b*) yields the averaged momentum equation

$$R\left[\partial_t q + \frac{6}{5}\partial_x\left(\frac{q^2}{h}\right)\right] = h\partial_{x^3}(h+s) + h - \frac{3q}{h^2} + \mathscr{A} + \mathscr{B} + \mathscr{C}, \qquad (4.6)$$

an evolution equation for q where

$$\mathscr{A} = -\partial_x \int_s^{s+h} \tau_{xx} \, \mathrm{d}y, \quad \mathscr{B} = -(\partial_x s)\tau_{xx}\big|_{y=s}, \quad \mathscr{C} - \frac{3q}{h^2} = \tau_{yx}\big|_{y=s}.$$

Details of the derivation procedure are given in Appendix B. $\mathscr{A}$ represents the contribution of the x-directed normal stress average across the film, $\mathscr{B}$ is an x-directed normal stress response on the wall induced by the topography and $\mathscr{C} - 3q/h^2$ is the wall shear stress. Using the expressions for the stresses in (4.2) gives

$$\mathscr{A} = 6De\partial_x\left(\frac{q^2}{h^3}\right), \quad \mathscr{B} = 18De\frac{q^2}{h^4}\partial_x s, \quad \mathscr{C} = De(\mathscr{C}_1 + \mathscr{C}_2),$$

where

$$\mathscr{C}_1 = 3\partial_t\left(\frac{q}{h^2}\right), \quad \mathscr{C}_2 = -18\frac{q^2}{h^4}\partial_x s.$$

All these terms are due to the viscoelasticity. $\mathscr{C}_2$ arises because of the topography and is the contribution of the y-directed normal stress to the wall shear stress. Notice that $De\mathscr{C}_2$ exactly cancels $\mathscr{B}$. As a consequence, the averaged momentum equation in (4.6) has a single non-homogeneous term, $-\partial_{x^3}s$, representing the additional capillary pressure induced by the topography and two viscoelastic forcing terms, $\mathscr{A}$ and $\mathscr{C}_1$. In the vicinity of the step, the capillary pressure gradient induced by the topography is $O(D/\delta^3)$ and is balanced by the pressure gradient due to the flow (see our discussion in §3).

Substituting now all the above terms into (4.6) yields

$$R\left[\partial_t q + \frac{6}{5}\partial_x\left(\frac{q^2}{h}\right)\right] = h\partial_{x^3}(h+s) + h - \frac{3q}{h^2} + 3De\left[2\partial_x\left(\frac{q^2}{h^3}\right) + \partial_t\left(\frac{q}{h^2}\right)\right]. \quad (4.7a)$$

Equation (4.7*a*) is complemented by the kinematic condition on the interface (2.7*b*) which, by integrating the continuity equation (2.6*c*) across the film, can be replaced

with

$$\partial_t h + \partial_x q = 0. \tag{4.7b}$$

Equations (4.7a) and (4.7b) are our final IBL system. Following Kalliadasis *et al.* (2000) we take the topography shape to be

$$s(x) = D\left[\frac{1}{2} - \frac{1}{\pi}\tan^{-1}\left(\frac{x}{\delta}\right)\right]. \tag{4.8}$$

For $De = 0$ and $s = 0$, (4.7) reduces to Shkadov's IBL approximation for a Newtonian film falling down a planar substrate (Shkadov 1967, 1968). The derivation of LWE from (4.7) is given in Appendix C.

4.1. *Linear stability of the Nusselt flat-film solution*

It is useful to examine the linear stability of the Nusselt flat-film solution far from the topographical feature. Consider infinitesimal perturbations in the form of normal modes

$$h = 1 + h'\exp(\lambda t + ikx), \quad q = \tfrac{1}{3} + \exp(\lambda t + ikx)$$

representing travelling waves in the streamwise direction with wavenumber k. The complex frequency $i\lambda = i\lambda_R - \lambda_I$ contains the growth rate λ_R, and the complex velocity $c = i\lambda/k$ with $c_R = -\lambda_I/k$ the phase velocity. Substituting these modes into (4.7) with $\partial_x s = 0$ and linearizing for $h', q' \ll 1$ yields a linear algebraic system with constant coefficients of the form $\boldsymbol{A}[h'q']^t = \boldsymbol{0}$ with $\boldsymbol{A}$ a 2×2 matrix. For the system to have non-trivial solutions, it is necessary and sufficient that its principal determinant be equal to zero. This yields an algebraic eigenvalue problem of the form $|\boldsymbol{A}| = 0$ which is the dispersion relation for λ as a function of k. For $R = O(1)$, the dispersion relation has two roots, which for $k \ll 1$ can be expanded as (it turns out that even terms of this expansion are real, and odd purely imaginary),

$$\lambda^1 \sim -ik + \tfrac{1}{3}\left(\tfrac{1}{3}R + De\right)k^2$$

and

$$\lambda^2 \sim -\frac{3}{R} - \frac{9}{R^2}De + \left(\frac{1}{5} + \frac{18}{5}\frac{De}{R}\right)ik - \frac{1}{3}\left(\frac{1}{3}R + De\right)k^2,$$

where the second root has been further expanded for $De \ll 1$.

The first root is an unstable mode corresponding to a surface wave propagating downstream with phase velocity $c_R^1 \sim 1 + O(k^2)$ and growth rate $\lambda_R^1 = (1/3)((1/3)R + De)k^2 + O(k^4)$. The growth rate curve saturates when we include terms of $O(k^4)$ and is characterized by an unstable band $0 \leqslant k \leqslant k_c$ containing the maximum growing wavenumber k_{max} and the cutoff wavenumber k_c. For example, with $R = 1$ and $De = 0.1$, $\lambda_R^1 \sim 0.144k^2 - 0.361k^4$ with $k_{max} \simeq 0.44$ and $k_c \simeq 0.64$. The second root is damped and corresponds to a surface wave propagating upstream with phase velocity $c_R^2 \sim -(1/5) - (18/5)(De/R) + O(k^2, De^2)$. For $R, De \ll 1$, the real part of the second root tends to $-\infty$, while the first root gives

$$\lambda^1 \sim -ik - \tfrac{1}{3}k^4 + \tfrac{1}{3}\left(\tfrac{1}{3}R + De\right)k^2.$$

For $De = R = 0$, this mode becomes $\lambda^1 = -ik - (1/3)k^4$. In this case, normal modes on the flat-film regions represent monochromatic waves that travel steadily with the kinematic wave velocity 1 and at the same time decay at the rate $-(1/3)k^4$.

Hence, viscoelasticity has a destabilizing influence on the Nusselt flat-film solution. We shall return to this point in §5 when we examine the time-dependent evolution of

the free surface. Note that for $De = 0$, we recover the classical Kapitza hydrodynamic mode of instability due to inertia for a film of a Newtonian liquid falling down a planar substrate (Kapitza 1948).

4.2. *Steady-state flows*

For steady-state flows, $\partial_t = 0$ and $h(x \rightarrow \pm\infty) = 1$, that is, perturbations of the free surface decay to the flat-film solution far upstream and downstream of the topographical feature. The steady version of (4.7b) then yields $q = \text{const}$ for all x, while the steady version of (4.7a) yields $q = 1/3$ as $x \rightarrow \pm\infty$ so that $q = 1/3$ for all x. The steady version of (4.7a) then becomes

$$\partial_{x^3}h = -\partial_{x^3}s + \frac{1 - h^3}{h^3} + \frac{2}{15h^5}(-Rh^2 + 15De)\partial_x h \qquad (4.9a)$$

subject to the boundary conditions

$$h(x \rightarrow \pm\infty) = 1. \qquad (4.9b)$$

The topography shape is given by (4.8). Notice that viscoelasticity affects the steady states through the single term $2De\partial_x h/h^5$ originating from $\mathscr{A}$ (which in turn originates from the average of the x-directed normal stress across the film). Finally, for $De = R = 0$, equation (4.9) reduces to that obtained by Kalliadasis *et al.* (2000) for non-inertial flows of Newtonian liquids over topography.

5. Results

The nonlinear ordinary differential equation, (4.9a), defining the steady states is solved numerically as a two-point boundary-value problem using the NAG solver D02GAF based on a finite-difference scheme with a deferred correction allied with a Newton iteration to solve the finite-difference equations. The accuracy of the numerical scheme is tested by varying the domain size and the initial mesh (the algorithm constructs the solution on a mesh defined by adding points to the initial uniform mesh with 10^4 points). Further, for Newtonian liquids in the absence of inertia ($R = De = 0$), we confirm the results obtained by Kalliadasis *et al.* (2000).

In all cases, the topographical shape is a step-down with $D = 1$. Figure 2(a) shows typical shapes for the profile $H(x) = h(x) + s(x)$ for fixed δ and R but different De. A domain $[-10, 10]$ with 10^4 points was found to be sufficient for the numerical solution to converge. Note that as we pointed out in §3, the long-wave assumption is satisfied for $Ca^{1/3}\partial_x s \ll 1$. For the values $\delta = 0.01$ and $D = 1$ in the figure, the quantity $Ca^{1/3}\partial_x s \sim Ca^{1/3}/\delta$ takes the value ~ 0.1 for $Ca \sim 10^{-9}$, i.e. close to the lower end of the range of capillary numbers given in §2. Hence, for the small value $\delta = 0.01$ the long-wave assumption is satisfied for very slow flows.

The figure indicates that viscoelastic flows over topography in the presence of inertia are also characterized by an asymmetric *capillary ridge* forming immediately before the step much like non-inertial flows of Newtonian liquids (Kalliadasis *et al.* 2000). Further, as figure 2(b) shows, there is a point immediately to the left of the step, where the deviation height h reaches a minimum, again much like non-inertial flows of Newtonian liquids (Kalliadasis *et al.* 2000). We shall be referring to this minimum as the *depression*. Note that, as was pointed out by Mazouchi & Homsy (2001), the ridge provides a capillary pressure gradient that is the only driving force for the flow once the ridge enters the step: indeed, in this region, the free surface is nearly perpendicular to the body force.
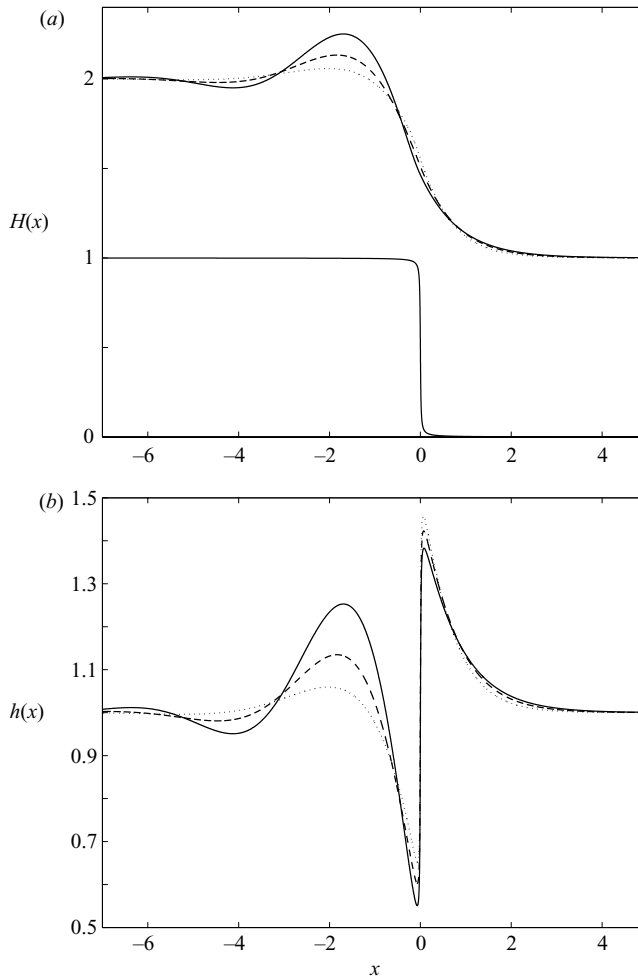
FIGURE 2. (*a*) Free-surface profiles $H(x) = h(x) + s(x)$ for a step-down in topography with $D = 1$, $\delta = 0.01$ and $R = 5$. (*b*) Deviation heights for the profiles in (*a*). —, $De = 0$; - - -, 0.4; $\cdots$, 1.0.

5.1. *On the steepness of the topography*

Figure 2(*b*) reveals that in the immediate vicinity of a sharp step, $\partial_x h$ is also large. Our computations indicate that $\partial_x h \sim \partial_x s \sim D/\delta$, as first mentioned in §3, so that for fixed D, the deviation height slope around the step is defined by δ, and $\partial_x h$ becomes large there because of the topography. In fact for a sharp step, $\partial_x s$ approaches $-\Delta(x)$ with $\Delta(x)$ a Dirac function at $x = 0$, and $\partial_x h$ approaches $\Delta(x)$ such that $\partial_x h \to -\partial_x s$. This observation was made first by Kalliadasis *et al.* (2000) in their study of flows over topography, but in the absence of inertia and viscoelasticity (see figure 8 in their paper). This limiting behaviour implies that the pressure gradient due to the flow cancels out the topography discontinuity: the only way to do that is with a discontinuity of the same form as that for the topography, but with opposite sign – the overall free-surface height cannot be discontinuous. The result is a smooth surface, as shown in figure 2(*a*).

Recall now from our discussion in §3 that even though the topography can be steep in the rescaled variables, in terms of the original dimensional variables, the topography depth is shallow compared to the topography scale. This was expressed by the condition $\tilde{D} \ll \tilde{\delta}$. The natural question then is why are we interested in the limit $\delta \ll 1$?

Mazouchi & Homsy (2001) solved the full Stokes equations for a Newtonian fluid over a step function ($\delta = 0$). This is the exact solution to the topography problem and hence correctly describes the flow regardless of the size of D. In fact, a comparison of the exact solution to that obtained with the LWE model developed by Kalliadasis *et al.* (2000) showed that for small Ca (roughly smaller than 10^{-2}) the LWE model is a valid approximation despite the substrate not being a small sloped topography. We expect the same to be true in our case, at least for weak inertia and viscoelasticity.

Hence, the simplified solution presented here based on the long-wave approximation should match, for small Ca and small δ, the solution of the full system without any approximations. This is because the simplified solution turns an originally smooth function into a sharp step function as $\delta \to 0$: both full solution and simplified solution solve for flow over a step in terms of dimensionless variables. It is then not surprising that the simplified solution should match the full one: although it converts a smooth function to a sharp step, the long-wave assumption is still obeyed as we emphasized in §3, and hence the model obtained based on the long-wave assumption should be accurate.

In other words, the full solution solves for flow over a sharp step both in terms of dimensional and dimensionless variables, and in terms of dimensionless variables the solution agrees with that obtained from the simplified model, provided that all conditions for the simplified model are met, i.e. $\tilde{D} \ll \tilde{\delta} \ll \ell$ and $h_0 \ll \ell(\tilde{D}/\tilde{\delta})$ (see §3). In terms of dimensional variables, the condition $\tilde{D} \ll \tilde{\delta} \ll \ell$ implies that the topography is shallow with a characteristic scale small compared to the capillary scale, and the condition $h_0 \ll \ell(\tilde{D}/\tilde{\delta})$ implies both $\partial_{\tilde{x}}\tilde{h} \ll \partial_{\tilde{x}}\tilde{s}$, i.e. the slope of the film far from the topography is small compared to the topography slope, and $1 \ll D/\delta$ for small δ. Also, $h_0 \ll \ell(\tilde{D}/\tilde{\delta})$ ensures $h_0 \ll \ell$ for a shallow topography, or equivalently, the capillary number must be small. For the step function, the conditions are simply $\tilde{D} \ll \ell$ and $h_0 \ll \ell$, or with $\tilde{D} \sim h_0$ used in the computations by Mazouchi & Homsy (2001), the capillary number must be small.

It is precisely for this reason that the steady states of the full Stokes equations for flow over a step function approach for small Ca those obtained from the LWE theory for small δ. Physically, for small Ca, the capillary length ℓ is so long compared to both $\tilde{D}$ and $\tilde{\delta}$ that the flow cannot tell the difference between a sharp step with depth $\tilde{D}$ and a mild topography with depth $\tilde{D}$ and width $\tilde{\delta}$: from the point of view of a coordinate system where the streamwise variation is measured in units of ℓ, the mild topography appears 'steep'.

Another way to put it is that the flow over a sharp step in terms of dimensional variables can be approximated with the flow over a much simpler smooth function when all conditions required for the simplified model are satisfied. (The precise functional form of the smooth function is immaterial as long as it leads to $\partial_x s \sim D/\delta \gg 1$). One can then solve for the flow using the simplified model, instead of the full model, thus greatly reducing the computational requirements.

5.2. *Influence of inertia and viscoelasticity*

Let us now discuss the influence of viscoelasticity. For a given R, increasing De and thus making the fluid increasingly non-Newtonian leads to a decrease of H_{max} as
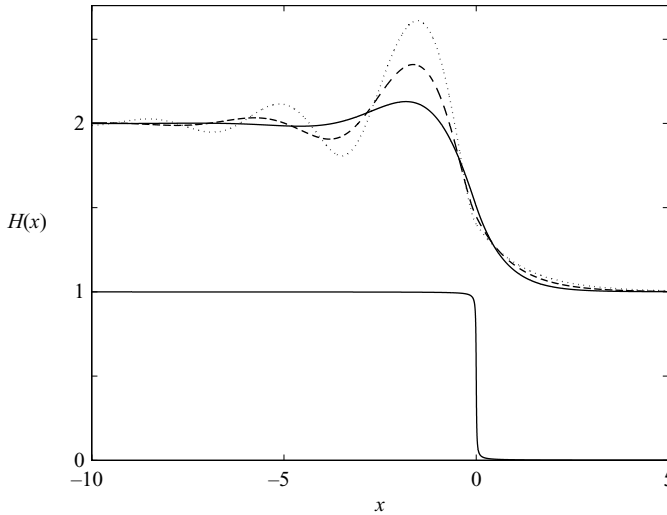
FIGURE 3. Free-surface profiles for —, $R = 0$; - - -, 15; $\cdots$, 25 with $De = 0.2$, $D = 1$ and $\delta = 0.01$.

shown in figure 2(a). In fact, our results suggest that with increasing De, the quantity $H_{max} - 1$ tends monotonically to zero, corresponding to a solution in which the free surface conforms closely to the topography. Of course, values as large as $De = 1$ and larger are beyond the region of validity of our perturbation expansion. Nevertheless, the question of an asymptotic behaviour of the free surface for large De is still a relevant one within the context of our model in (4.9) (and, in fact, on many occasions perturbation theories can provide a good approximation beyond the region of their validity).

Hence, viscoelastic fluids have smaller ridges compared to Newtonian ones. In that respect, the situation here is then similar to that of another thin-film problem that exhibits ridges: that of viscoelastic contact lines driven by body forces (Spaid & Homsy 1994, 1996) where the viscoelastic effects tend to reduce the height of the ridge (for sufficiently small values of the precursor film thickness). However, the mechanism for the reduction of the ridge in our case is different to that for viscoelastic contact lines (see Spaid & Homsy (1994) for a detailed analysis of the mechanism in the contact-line problem): it is because the maximum velocity gradients and hence shear in our system occur in the vicinity of the depression (where the deviation height is a minimum). The polymeric molecules then experience maximum stretching around the depression, resulting in maximum contraction of the molecules there, which then gives rise to increasing x-directed normal stresses (the contraction pulls against the shear stress that stretches the molecules) which in turn lead to expansion/thickening of the fluid in the vicinity of the step and hence to reduction of the depression (recall also from §4.2 that viscoelasticity affects the steady states through the x-directed normal stresses only). A diminished depression corresponds to a smaller ridge owing to conservation of mass in the system expressed by the invariance $\int_{-\infty}^{+\infty} (1 - h^3)/h^3 \mathrm{d}x = 0$ which is guaranteed from (4.9a) using (4.9b) (this property implies that if $h > 1$ in a certain domain, we must have $h < 1$ in another domain so that $(1 - h^3)/h^3$ can change sign from < 0 to > 0 and the integral vanishes).

Figure 3 shows the influence of inertia on flows over a step-down. A domain $[-20, 10]$ with 8×10^4 (starting from 10^4) points was found to be sufficient for the
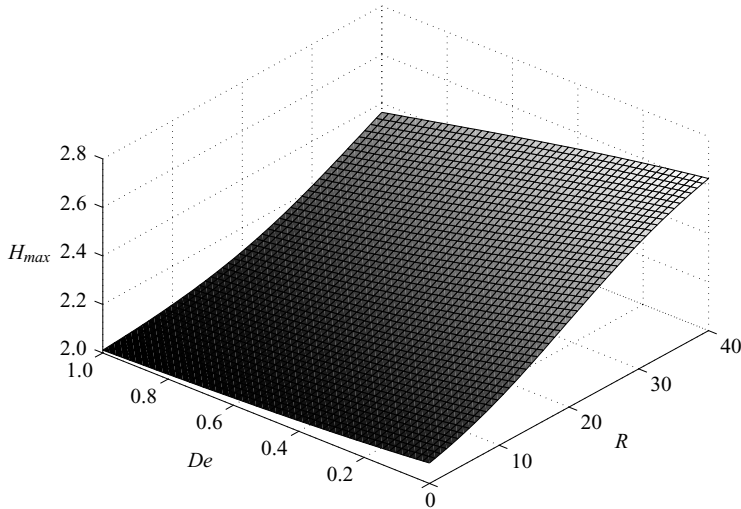
FIGURE 4. H_{max} as a function of *De* and *R* for $D = 1$ and $\delta = 0.2$.

numerical solution to converge. The bigger domain in figure 3 compared to that in figure 2 is due to the presence of the long oscillations at the back of the capillary ridge. Increasing *R* leads to an amplification of the capillary ridge. The capillary oscillations to the back of the ridge are also enhanced – a signature of finite inertia in the system (and hence energy dissipation on short wavelengths). Hence, unlike *De* whose influence is local and limited around the capillary ridge, *R* influences a much larger region of the flow. Figure 4 is a two-dimensional plot of H_{max} as a function of both *De* and *R*. Evidently, the higher capillary ridges appear for small *De* and large *R*.

Finally, the maximum height of the capillary ridge H_{max} for $De = 0$ in figure 2(*a*) is ~ 2.25 larger than both the LWE result with $R = De = 0$, $H_{max} \sim 2.18$, and the Stokes flow result with $R = De = 0$ by Mazouchi & Homsy (2001), $H_{max} \sim 2.16$ at $Ca = 0.025$. This increase is purely an inertial effect. On the other hand, the maximum height of the capillary ridge for $R = 0$ in figure 3(*a*) is ~ 2.14 smaller than both the LWE result with $R = De = 0$, $H_{max} \sim 2.18$, and the Stokes flow result with $R = De = 0$ by Mazouchi & Homsy (2001), $H_{max} \sim 2.16$ at $Ca = 0.025$. This decrease is purely a viscoelastic effect.

5.3. *Time-dependent evolution: interaction of a solitary pulse with the capillary ridge*

Figure 5 depicts the time evolution obtained from (4.7) for $R = 3$, $De = 0.1$, $D = 1$ and $\delta = 0.1$. Our numerical scheme is fully implicit in time with projections of *h* and *q* onto cubic and linear splines, respectively (owing to the order of the highest derivatives for these two functions being 3 and 1, respectively) and the time derivatives of *h* and *q* approximated by forward finite differences. At every time step, we obtain a set of nonlinear algebraic equations that we solve using Newton's method. We dynamically choose the time step to avoid using unnecessarily small time steps. The accuracy of the numerical scheme is determined by variation of domain size and number of points in the domain.

The boundary conditions are inlet conditions at the left-hand end of the domain with $h = 1$, $q = 1/3$ and $h = 1$, $\partial_x h = 0$ at the exit. Clearly, the last boundary condition is not appropriate when interfacial disturbances approach the exit and in this case
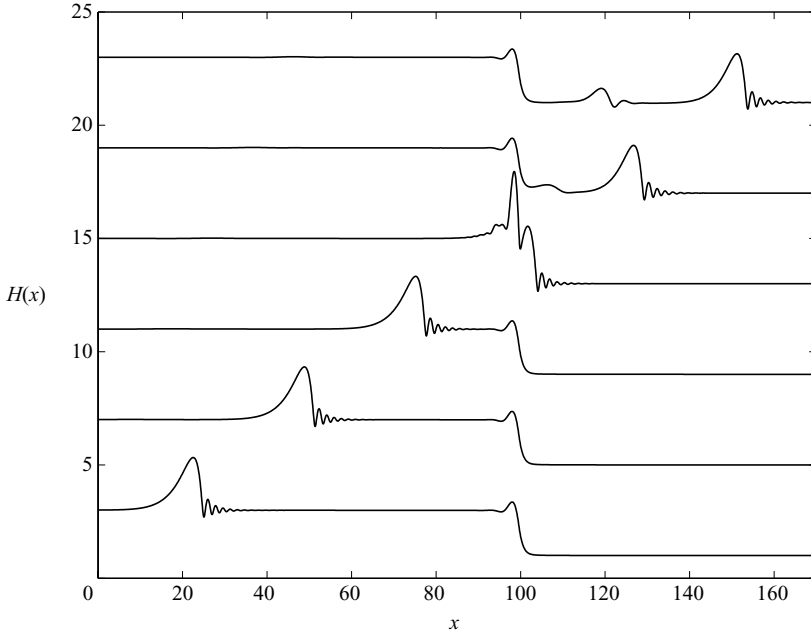
FIGURE 5. Time evolution for the free surface in an extended domain obtained from (4.7) for $R = 3$, $De = 0.1$, $D = 1$ and $\delta = 0.1$. The vertical axis marks the height of the total free-surface height H for the bottom curve. Successive curves are separated by space intervals $\Delta H = 4$ in the vertical direction and time intervals $\Delta t = 10$ with $t \in [0, 50]$. At $t = 50$, a second soliton is already visible behind the original one.

it must be replaced with a 'soft boundary condition' that would minimize upstream feedback. However, here we are primarily interested in the evolution of the interface around the capillary ridge (which for sufficiently long domains is not influenced by the actual condition at the exit). The initial condition is taken to be $h_s + \hat{h}_s - 1$ where h_s denotes the steady state for flow over topography and $\hat{h}_s$ a solitary wave on a substrate of thickness 1. This solitary wave is obtained from a time-dependent computation using the same boundary conditions as those in figure 5. The initial condition is a Gaussian distribution.

The shape of the solitary pulse on the surface of a film falling down a planar substrate and in the presence of inertia and viscoelasticity is qualitatively similar to that of solitary pulses for Newtonian films falling down a planar substrate (e.g. Chang & Demekhin 2002; Ruyer-Quil & Manneville 2002). This 'generic' solitary wave shape consists of a big hump with a gently sloping back edge and a steep front edge preceded by a series of small decaying bow waves. However, the amplitude of the viscoelastic solitary wave relative to its substrate for the conditions in figure 5 is $\simeq 2.35$, $\simeq 10\%$ larger than the value $\simeq 2.05$ of the corresponding Newtonian solitary wave. This is consistent with our linear stability analysis in §4.1 which showed that viscoelasticity has a destabilizing influence on films falling down planar substrates (recall from this section that normal modes on the flat-film regions represent infinitesimal monochromatic waves travelling downstream with the kinematic wave velocity $c_R^1 \sim 1$ and growth rate $\lambda_R^1 \sim (1/3)((1/3)Re + De)k^2$). The basic instability mechanism for a film on a flat substrate is the same as that causing the reduction of the depression discussed earlier: the normal stresses induced by stretching the

polymeric molecules with the shear flow cause an expansion of the fluid. Note also that for the value of R in figure 5, the LWE model obtained in Appendix C blows up in finite time (see also our discussion in §1).

The solitary pulse at $t = 0$ in figure 5 is slightly 'excited', i.e. it has a larger amplitude than that corresponding to the parameter values of the figure. This is because the non-stationary computation was deliberately not performed for very large times; had we done this, our pulse would have approached a stationary equilibrium pulse asymptotically in time. Hence, we have a quasi-equilibrium pulse that carries an additional amount of mass compared to the equilibrium one. The velocity of the pulse is $\simeq 2.5$, i.e. $\simeq 2.5$ times that of the kinematic wave velocity. As the pulse travels, the excess mass drains to the back of the pulse causing its decay. This draining mass grows exponentially behind the pulse forming a tail in this region. The drainage process has a slow dynamics and hence the exponential growth of the tail to the back is small. As a consequence, the tail is not really visible in the snapshots of figure 5 for $t = 0, 10, 20$. Hence, the situation here is similar to that of solitary pulses on Newtonian falling films. In this case, Chang, Demekhin & Kalaidin (1998) and Chang & Demekhin (2002) have demonstrated that the tail region is driven by a 'resonance pole' mode. A similar mode was uncovered by Kalliadasis *et al.* (2003*a*) in the problem of a falling film heated from below by a local heat source. Such modes are not true eigenmodes of the linearized eigenvalue problem that governs the stability of the solitary pulses since they exhibit unbounded behaviour as $x \to -\infty$. However, they can be regarded as true eigenvalues of an appropriate weighted space (see also Chang, Demekhin & Saprykin 2002; Kalliadasis *et al.* 2003*a*). It is likely that in our case such resonance poles are responsible for determining the decay rate and drainage dynamics of excited viscoelastic solitary pulses; however, a detailed analysis of these modes would require investigation of the linearized eigenvalue problem governing the stability of the pulses, which is beyond the scope of the present study.

The draining excited pulse will eventually meet the capillary ridge. At $t = 30$, the pulse is right on top of the ridge. Note that relative to the pulses for $t = 0, 10, 20$, the width of the pulse for $t = 30$ is smaller and its amplitude relative to the surrounding free surface larger. The mechanism for the formation of this narrow pulse is not related to viscoelasticity. In fact, it is exactly the same to that for the formation of the ridge, as discussed earlier: the fluid bunches up before the entry to the step so that it can enter the step. The step then influences the solitary pulse in exactly the same way as the fluid in the capillary ridge. We then have a pulse which is more excited and further disturbed from its equilibrium and, as a consequence, the drainage process is now faster. The solitary wave then sheds the excess mass prior to entering the step. (Note that the excess mass that drains behind the pulse immediately before the pulse enters the step is due to the further excitation of the pulse by the same mechanism responsible for ridge formation and should not be confused with the mass that drains slowly to the back of the slightly excited pulse before it meets the ridge. This mass continues to be present on the flat film behind the ridge for $t = 30, 40, 50$ and moves slowly from left to right.) This mass is already visible immediately behind the solitary wave for $t = 30$. It also travels from left to right following the primary soliton, but at a lower speed and so it lags behind. It is visible in the snapshot for $t = 40$ right at the front of the capillary ridge (but some of it still remains on the ridge which for $t = 40$ has a slightly larger amplitude than the steady-state value). This mass forms a small soliton at $t = 50$ by sucking liquid from the front substrate and the small amount of mass around the ridge at $t = 40$ that eventually drains out of it. This soliton will eventually grow to a stationary equilibrium pulse (by continuously sucking liquid
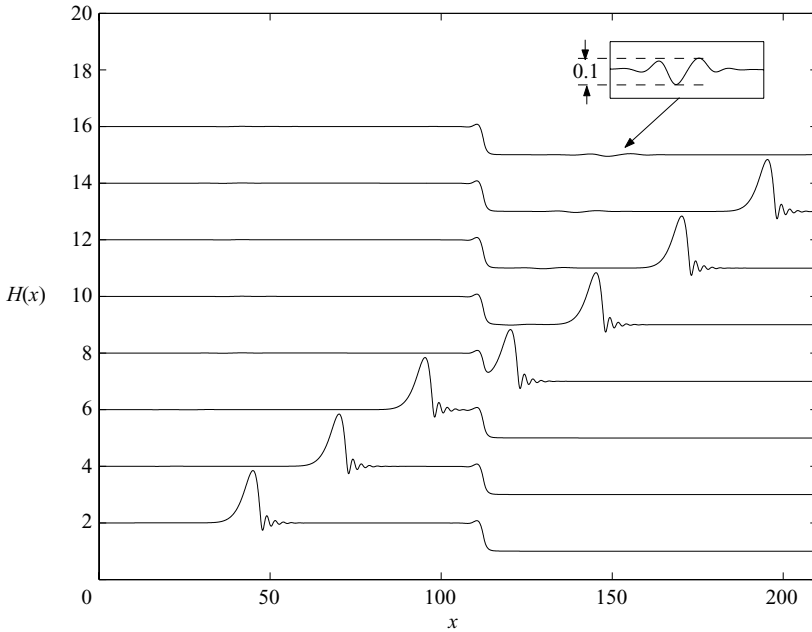
FIGURE 6. Time evolution for the free surface in an extended domain obtained from (4.7) for $R = 1$, $De = 0.3$, $D = 1$ and $\delta = 0.1$. The vertical axis marks the height of the total free-surface height H for the bottom curve. Successive curves are separated by space intervals $\Delta H = 2$ in the vertical direction and time intervals $\Delta t = 10$ with $t \in [0, 70]$. The inset shows a wave packet at $t = 70$ with amplitude $\simeq 0.1$ representing the first stages of the development of a second soliton behind the original one.

from the front substrate) of the same amplitude and speed as the original pulse which has now travelled near the end of the domain for $t = 50$ (there is no more drainage from this pulse).

Hence, the presence of the capillary ridge accelerates the drainage process of an excited solitary pulse and breaks the resonance poles – drainage law for solitary pulses on planar substrates. For the parameter values in figure 5, the drainage process is controlled by inertia while the role of viscoelasticity is restricted to increasing the height of the solitary pulse and reducing the height of the ridge.

The capillary ridge eventually recovers its steady-state configuration as soon as the excess mass is convected away from the step-down. This then indicates that viscoelastic capillary ridges are strongly stable, much like ridges in non-inertial flows of Newtonian liquids over topography (Kalliadasis & Homsy 2001; Davis & Troian 2005). The mechanism for this strong stability must be the same as Newtonian ridges, i.e. the capillary pressure induced by the topography acts as a strong restoring force that brings the ridge back to its original shape (Kalliadasis & Homsy 2001).

Figure 6 shows the time-evolution obtained from (4.7) for $R = 1$, $De = 0.3$ and with the remaining parameters the same with those in figure 5. Both inertia and viscoelasticity now contribute to the evolution and the drainage process. The soliton travels with a velocity $\simeq 2.5$, close to that for the soliton in figure 5. The drainage process is similar to that occurring in figure 5, but the growth of the second soliton behind the original one is slower to that in figure 5. Indeed, for the parameter values of figure 5, the maximum growth rate is $\lambda_{max} \simeq 0.06$ whereas for the parameter values of figure 6, $\lambda_{max} \simeq 0.032$. On the other hand, for figure 5, $k_{max} \simeq 0.65$, and for figure 6,
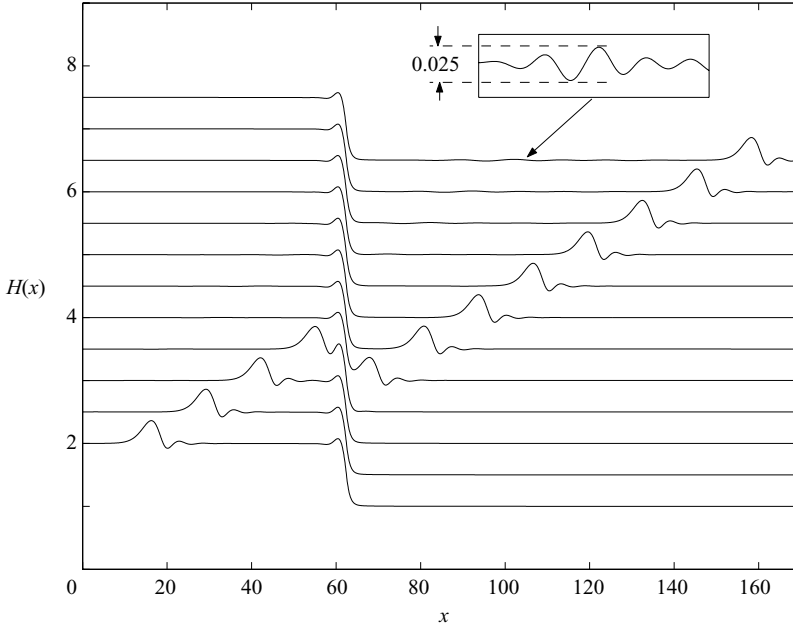
FIGURE 7. Time evolution for the free surface in an extended domain obtained from (4.7) for $R = 10^{-4}$, $De = 0.3$, $D = 1$ and $\delta = 0.1$. The vertical axis marks the height of the total free-surface height H for the bottom curve. Successive curves are separated by space intervals $\Delta H = 0.5$ in the vertical direction and time intervals $\Delta t = 10$ with $t \in [0, 110]$. The inset shows a wave packet at $t = 110$ with amplitude $\simeq 0.025$ representing the onset of the creation of a second soliton behind the original one.

$k_{max} \simeq 0.56$, so that the maximum growing wavenumber does not change significantly. The excess mass that the original soliton sheds prior to entering the step travels to the front of the step and eventually starts to grow into a wave packet, shown for $t = 70$ in the inset of the figure. The second soliton is created within this wave packet.

Solitary waves on the surface of a viscoelastic film falling down a planar substrate can exist even in the absence of inertia. These waves resemble the inertia-driven solitary waves on Newtonian liquids. Figure 7 depicts the time evolution obtained from (4.7) for $R = 10^{-4}$, $De = 0.3$ and with the remaining parameters the same as those in figure 5. The evolution is now driven primarily by viscoelasticity. The soliton travels with a velocity $\simeq 1.5$ and is slower than both solitons in figures 5 and 6. Its amplitude is also smaller than that in figures 5 and 6. The drainage events resulting from the interaction of an excited solitary pulse with the capillary ridge are similar to those observed in figure 5. The growth of the second soliton behind the original one is slower than that in figure 6 as now $\lambda_{max} \simeq 0.0076$; however, $k_{max} \simeq 0.4$, and it has not changed significantly from both figures 5 and 6. The second soliton is born out of the wave packet shown in the inset of the figure for $t = 110$.

6. Summary

We have examined the influence of inertia and viscoelasticity on free-surface thin-film flows over topography by using the flow over a step-down as a prototype. The viscoelastic behaviour was modelled with the convected Maxwell constitutive equation. Our analysis was based on the integral-boundary-layer approximation of

the Navier–Stokes equation and wall/free-surface boundary conditions whereas the influence of the viscoelastic effects was examined via a perturbation theory for small Deborah numbers. The final model consists of two nonlinear partial differential equations for the evolution in time and space of the local deviation height and local flow rate.

We considered both steady states and time-dependent flows. We showed that steady states are characterized by an asymmetric capillary ridge before the entrance to the step-down and a depression immediately before the step-down much like Newtonian flows over topography. The maximum height of the ridge decreases monotonically as the Deborah number increases. This is because the normal stresses are more pronounced for large Deborah numbers, leading to a reduction of the depression and hence reduction of the ridge. These normal stresses are a direct consequence of the stretching that the polymeric molecules experience owing to the shear flow which has maximum velocity gradients in the vicinity of the step. Thus, the depression reduction/ridge reduction is effectively a shear-stress relief mechanism. On the other hand, increasing the modified Reynolds number leads to a monotonic amplification of the ridge and enhances the capillary oscillations to the back of the ridge.

Further, we investigated the interaction of inertia/viscoelasticity-driven quasi-stationary solitons with capillary ridges and we demonstrated that ridges have a dramatic influence on the drainage dynamics of excited pulses. This interaction is non-trivial. When an excited solitary pulse coalesces with the capillary ridge it becomes much more excited owing to exactly the same mechanism that is responsible for the formation of the capillary ridge. This then induces a fast drainage process by which the pulse sheds its excess mass prior to passing over the step-down. Once the pulse has travelled over the topographical feature, it becomes an equilibrium stationary solitary wave no longer excited. The ridge is disturbed during the coalescence event with the soliton, but once the soliton passes over the feature, it recovers its original shape. This demonstrates that viscoelastic capillary ridges are stable, much like their Newtonian counterparts. The solitary pulse also retains its stability and is not destroyed by the capillary ridge unlike e.g. radiation wave packets in Newtonian flows that can even destabilize a linearly stable pulse (Chang *et al.* 1998) (unless the pulse outruns the expanding growing wave packet).

Appendix A. Scales for the stresses

Here we discuss the scales for the stresses. Consider the non-dimensionalization:

$$\tau_{xx} \to a\tau_{xx}, \quad \tau_{yx} \to b\tau_{yx}, \quad \tau_{yy} \to c\tau_{yy}.$$

By using the non-dimensionalization in (2.5) with $\ell = h_0/Ca^{1/3}$ the capillary scale discussed in §2, the constitutive model in (2.4) becomes:

$$\tau_{xx} + De\left(\partial_t\tau_{xx} + u\partial_x\tau_{xx} + v\partial_y\tau_{xx} - 2\tau_{xx}\partial_x u - 2Ca^{-1/3}\frac{b}{a}\tau_{yx}\partial_y u\right) = -2\frac{\mu U}{a\ell}\partial_x u, \quad (A\,1a)$$

$$\tau_{yx} + De\left(\partial_t\tau_{yx} + u\partial_x\tau_{yx} + v\partial_y\tau_{yx} - Ca^{1/3}\frac{a}{b}\tau_{xx}\partial_x v - Ca^{-1/3}\frac{c}{b}\tau_{yy}\partial_y u\right)$$
$$= -\frac{\mu U}{bh_0}\left(\partial_y u + Ca^{2/3}\partial_x v\right), \quad (A\,1b)$$

$$\tau_{yy} + De\left(\partial_t\tau_{yy} + u\partial_x\tau_{yy} + v\partial_y\tau_{yy} - 2Ca^{1/3}\frac{b}{c}\tau_{xy}\partial_x v - 2\tau_{yy}\partial_y v\right) = -2\frac{\mu U}{c\ell}\partial_y v. \quad (A\,1c)$$

The scale for the τ_{yx} stress can be readily identified: from (2.4b) $\tau_{yx} \sim \mu\partial_y u$ or $\tau_{yx} \sim \mu U/h_0$ and hence $b = \mu U/h_0$ so that the shear stress and the component d_{12} of the rate-of-strain tensor are of the same order; this is the usual scale for the shear stress in interfacial flows. To obtain the scales for the normal stresses τ_{xx} and τ_{yy}, we require that the time-dependent and nonlinear terms in the left-hand side of (A1) balance. As a consequence, all nonlinear terms in the left-hand side of (A1) are multiplied by the Deborah number De only, which is after all a measure of the nonlinearities in the constitutive model for the stresses (Bird *et al.* 1987). This gives:

$$Ca^{-1/3}\frac{b}{a} \sim 1, \quad Ca^{1/3}\frac{a}{b} \sim Ca^{-1/3}\frac{c}{b}, \quad Ca^{1/3}\frac{b}{c} \sim 1,$$

or

$$a = \frac{\mu U\ell}{h_0^2}, \quad c = \frac{\mu U}{\ell}.$$

At the same time, the above order-of-magnitude assignments are necessary in order to obtain a well-defined thin-film limit. In fact, these are the only scales allowing us to do so.

Appendix B. Derivation of the IBL system

We first average the left-hand side of (4.1):

$$\int_s^H (\partial_t u + u\partial_x u + v\partial_y u)\,\mathrm{d}y = \int_s^H \partial_t u\,\mathrm{d}y + \int_s^H u\partial_x u\,\mathrm{d}y + \int_s^H v\partial_y u\,\mathrm{d}y. \quad (B\,1)$$

The first term in the right-hand side of (B1) is evaluated by applying the Leibnitz rule and the no-slip condition (2.7a). The last term in (B1) is evaluated by performing integrations by parts, using the continuity equation (2.6) and the no-slip condition (2.7a). The right-hand side of (B1) can then be written as:

$$\partial_t \int_s^H u\,\mathrm{d}y + u|_{y=H}(v|_{y=H} - \partial_t H) + 2\int_s^H u\partial_x u\,\mathrm{d}y,$$

which by using the kinematic boundary condition (2.7b), and applying the Leibnitz rule yields:

$$\partial_t \int_s^H u\,\mathrm{d}y + 2\int_s^H \tfrac{1}{2}\partial_x(u^2)\mathrm{d}y + (u|_{y=H})^2\partial_x H = \partial_t \int_s^H u\,\mathrm{d}y + \partial_x \int_s^H u^2\,\mathrm{d}y.$$

The two terms on the right-hand side of this equation can be evaluated easily by using the velocity profile in (4.3a) and the definition of the flow rate in (4.3b). Equation (B1) then becomes:

$$\int_s^H (\partial_t u + u\partial_x u + v\partial_y u)\,\mathrm{d}y = \partial_t q + \tfrac{6}{5}\partial_x\left(\frac{q^2}{h}\right). \quad (B\,2)$$

We now turn to the averaging of the right-hand side of (4.1):

$$\int_s^H (\partial_{x^3} H - \partial_x \tau_{xx} - \partial_y \tau_{yx} + 1)\, \mathrm{d}y = h\partial_{x^3} H - \int_s^H \partial_x \tau_{xx}\, \mathrm{d}y - \int_s^H \partial_y \tau_{yx}\, \mathrm{d}y + h. \quad \text{(B 3)}$$

To evaluate the first integral in the right-hand side of (B 3), we use the Leibnitz rule and the identity $\tau_{xx}|_{y=H} = 0$ with the velocity test function we have adopted. Hence,

$$\int_s^H \partial_x \tau_{xx}\, \mathrm{d}y = \partial_x \int_s^H \tau_{xx}\, \mathrm{d}y + (\partial_x s)\, \tau_{xx}|_{y=s}.$$

The evaluation of the second integral on the right-hand side of (B 3) is straightforward. Equation (B 3) then becomes:

$$\int_s^H (\partial_{x^3} H - \partial_x \tau_{xx} - \partial_y \tau_{yx} + 1)\, \mathrm{d}y$$

$$= h\partial_{x^3} H - \partial_x \int_s^H \tau_{xx}\, \mathrm{d}y - (\partial_x s)\, \tau_{xx}|_{y=s} + \tau_{yx}|_{y=s} + h. \quad \text{(B 4)}$$

Equating now the right-hand side of (B 2) multiplied by R to the right-hand side of (B 4) yields (4.6).

Appendix C. Derivation of LWE from the IBL system

LWE can be derived from the IBL system in (4.7) by performing a gradient expansion of the form

$$q = q_0 + q_1 + \cdots$$

with $q_{n+1} \ll q_n$. q_{n+1} can be obtained from the iterative scheme

$$R\left[\partial_t q_n + \tfrac{6}{5}\partial_x \left(\frac{q_n^2}{h}\right)\right] = h\partial_{x^3} H + h - \frac{3q_{n+1}}{h^2} + 3De\left[2\partial_x \left(\frac{q_n^2}{h^3}\right) + \partial_t \left(\frac{q_n}{h^2}\right)\right] \quad (n = 0, 1, 2, \ldots),$$

where $q_0 = h^3/3$. A single iteration with $n = 0$ then yields

$$q_1 = \tfrac{1}{3}h^3 + \tfrac{1}{3}h^3\partial_{x^3} H + \tfrac{1}{9}Rh^6\partial_x h + \tfrac{1}{3}Deh^4\partial_x h.$$

Substituting $q_{0,1}$ into $\partial_t h + \partial_x[q_0 + q_1] = 0$ gives the LWE model,

$$\partial_t h + \tfrac{2}{3}\partial_x(h^3) + \tfrac{1}{3}\partial_x \left(\tfrac{1}{3}Rh^6\partial_x h + Deh^4\partial_x h + h^3\partial_{x^3} H\right) = 0,$$

which is precisely the equation obtained directly from a long-wave approximation of the equations of motion and wall/free-surface boundary conditions.

The second term in the above equation is the convective term due to mean flow, the third and fourth terms are due to inertia and viscoelasticity, respectively, and the fifth term is the streamwise curvature gradient that accounts for both the deviation height and substrate curvatures. Hence, in the lubrication limit the viscoelastic contribution is similar to the inertial one, but with a power of 4 for h instead of 6.

REFERENCES

ARGYRIADI, K., VLACHOGIANNIS, M. & BONTOZOGLOU, V. 2006 Experimental study of inclined film flow along periodic corrugations: the effect of wall steepness. *Phys. Fluids* **18**, 012102.

BIELARZ, C. & KALLIADASIS, S. 2003 Time-dependent free-surface thin film flows over topography. *Phys. Fluids* **15**, 2512–2524.

BIRD, R. B., ARMSTRONG, R. C. & HASSAGER, O. 1987 *Dynamics of Polymeric Liquids. Volume 1: Fluid Mechanics*. Wiley.

CHANG, H.-C. 1994 Wave evolution on a falling film. *Annu. Rev. Fluid Mech.* **26**, 103–136.

CHANG, H.-C. & DEMEKHIN, E. A. 2002 *Complex Wave Dynamics on Thin Films*. Elsevier.

CHANG, H.-C., DEMEKHIN, E. A. & KALAIDIN, E. 1998 Generation and suppression of radiation by solitary pulses. *SIAM J. Appl. Maths* **58**, 1246–1277.

CHANG, H.-C., DEMEKHIN, E. A. & SAPRYKIN, S. 2002 Noise-driven wave transitions on a vertically falling film. *J. Fluid Mech.* **462**, 255–283.

DAVIS, J. M. & TROIAN, S. M. 2005 Generalized linear stability of noninertial coating flows over topographical features. *Phys. Fluids* **17**, 072103.

FERNANDEZ-PARENT, C., LAMMERS, J. H. & DECRÉ, M. M. J. 1998 Flow of a gravity driven thin liquid film over one-dimensional topographies. *Philips Res. Unclassified Rep.* UR 823/98.

FRAYSSE, N. & HOMSY, G. M. 1994 An experimental study of rivulet instabilities in centrifugal spin coating of viscous Newtonian and non-Newtonian fluids. *Phys. Fluids* **6**, 1491–1504.

GRAMLICH, C. M., KALLIADASIS, S., HOMSY, G. M. & MESSER, C. 2002 Optimal levelling of flow over one-dimensional topography by Marangoni stresses. *Phys. Fluids* **14**, 1841–1850.

KALLIADASIS, S. & HOMSY, G. M. 2001 Stability of free-surface thin-film flows over topography. *J. Fluid Mech.* **448**, 387–410.

KALLIADASIS, S., BIELARZ, C. & HOMSY, G. M. 2000 Steady free-surface thin film flows over topography. *Phys. Fluids* **12**, 1889–1898.

KALLIADASIS, S., KIYASHKO, A. & DEMEKHIN, E. A. 2003a Marangoni instability of a thin liquid film heated from below by a local heat source. *J. Fluid Mech.* **475**, 377–408.

KALLIADASIS, S., DEMEKHIN, E. A., RUYER-QUIL, C. & VELARDE M. G. 2003b Thermocapillary instability and wave formation on a film falling down a uniformly heated plane. *J. Fluid Mech.* **492**, 303–338.

KAPITZA, P. L. 1948 Wave flow of thin layers of a viscous fluid. I. Free flow. *Sov. Phys., J. Exp. Theor. Phys.* **18**, 3–18.

KHAYAT, R. E. 2000 Transient two-dimensional coating flow of a viscoelastic fluid film on a substrate of arbitrary shape. *J. Non-Newtonian Fluid Mech.* **95**, 199–233.

MAZOUCHI, A. & HOMSY, G. M. 2001 Free surface Stokes flow over topography. *Phys. Fluids* **13**, 2751–2761.

MESSÉ, S. & DECRÉ, M. M. J. 1997 Experimental study of a gravity driven water film flowing down inclined plates with different patterns. *Philips Res. Uncliasified Rep.* UR 030/97.

ORON, A. & GOTTLIEB, O. 2002 Nonlinear dynamics of temporally excited falling liquid films. *Phys. Fluids* **14**, 2622–2636.

PUMIR, A., MANNEVILLE, P. & POMEAU, Y. 1983 On solitary waves running down an inclined plane. *J. Fluid Mech.* **135**, 27–50.

ROSENAU, P., ORON, A. & HYMAN, J. M. 1992 Bounded and unbounded patters of the Benney equation. *Phys. Fluids* A **4**, 1102–1104.

RUYER-QUIL, C. & MANNEVILLE, P. 2000 Improved modeling of flows down inclined planes. *Eur. Phys. J.* B **15**, 357–369.

RUYER-QUIL, C. & MANNEVILLE, P. 2002 Further accuracy and convergence results of the modeling of flows down inclined planes by weighted residual approximations. *Phys. Fluids* **14**, 170–183.

RUYER-QUIL, C., SCHEID, B., KALLIADASIS, S., VELARDE, M. G. & ZEYTOUNIAN, R. KH. 2005 Thermocapillary long waves in a liquid film flow. Part 1. Low-dimensional formulation. *J. Fluid Mech.* **538**, 199–222.

SCHEID, B., RUYER-QUIL, C., THIELE U., KABOV, O. A., LEGROS, J. C. & COLINET, P. 2004 Validity domain of the Benney equation including Marangoni effect for closed and open flows. *J. Fluid Mech.* **527**, 303–335.

SCHEID, B., RUYER-QUIL, C., KALLIADASIS, S., VELARDE, M. G. & ZEYTOUNIAN, R. KH. 2005 Thermocapillary long waves in a liquid film flow. Part 2. Linear stability and nonlinear waves. *J. Fluid Mech.* **538**, 223–244.

SHKADOV, V. YA 1967 Wave models in the flow of a thin layer of a viscous liquid under the action of gravity. *Izv. Akad. Nauk SSSR, Mekh. Zhid. i Gaza* **1**, 43–50.

SHKADOV, V. YA 1968 Theory of wave flow of a thin layer of a viscous liquid. *Izv. Akad. Nauk SSSR, Mekh. Zhid. i Gaza* **2**, 20–25.

Spaid, M. A. & Homsy, G. M. 1994 Viscoleastic free surface flows: spin coating and dynamic contact lines. *J. Non-Newtonian Fluid Mech.* **55**, 249–281.

Spaid, M. A. & Homsy, G. M. 1996 Stability of Newtonian and viscoelastic dynamic contact lines. *Phys. Fluids* **8**, 460–478.

Stillwagon, L. E. & Larson, R. G. 1988 Fundamentals of topographic substrate leveling. *J. Appl. Phys.* **63**, 5251–5258.

Stillwagon, L. E. & Larson, R. G. 1990 Leveling of thin films over uneven substrate during spin coating. *Phys. Fluids* **2**, 1937–1944.

Zhang, Y. L., Matar, O. K. & Craster, R. V. 2002 Surfactant spreading on a thin weakly viscoelastic film. *J. Non-Newtonian Fluid Mech.* **105**, 53–78.